Electronic Supplementary Material (ESI) for Catalysis Science & Technology.

CO_2 Chemisorption and Activation on Carbon Nitride with Less Amino Groups Boosts CO_2 Photoreduction

Debin Zeng[a,1], Xiting Wang[a,1], Chunguang Kuai[a], Zhuo Jiang[a],* and Yuzheng Guo[a],*

[a]*School of Electrical Engineering and Automation, Wuhan University, Wuhan, 430072, PR, China*

*Corresponding authors

E-mail: zhuojiang@whu.edu.cn; yguo@whu.edu.cn

[1]These authors contributed equally to this work.

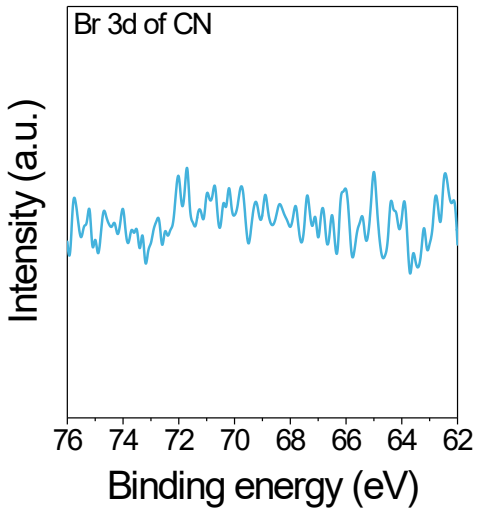

Figure S1. X-ray photoelectron spectra (XPS) of Br *3d*.

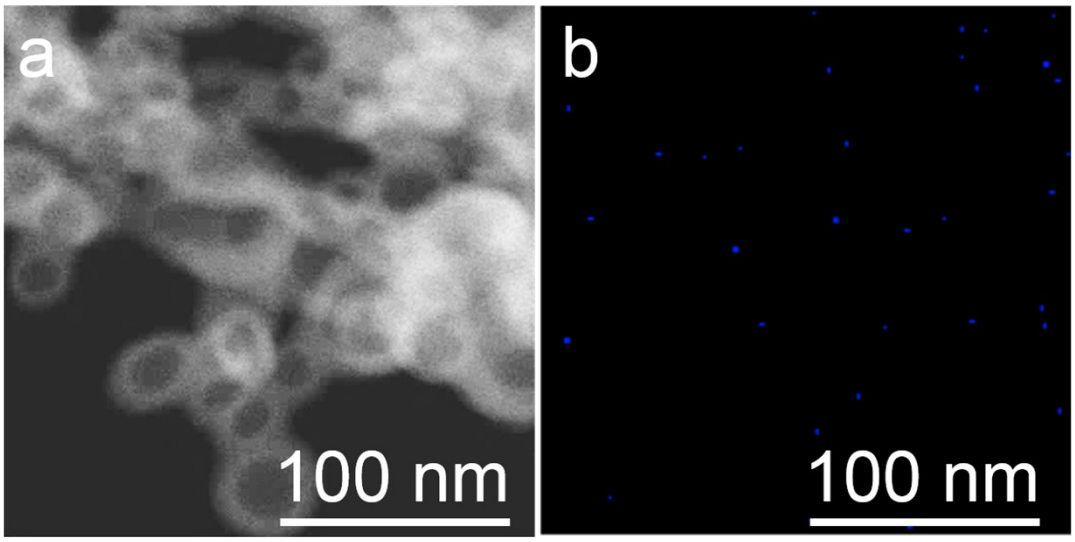

Figure S2. a) Scanning transmission electron microscope (STEM) image. **b)** Elemental mapping.

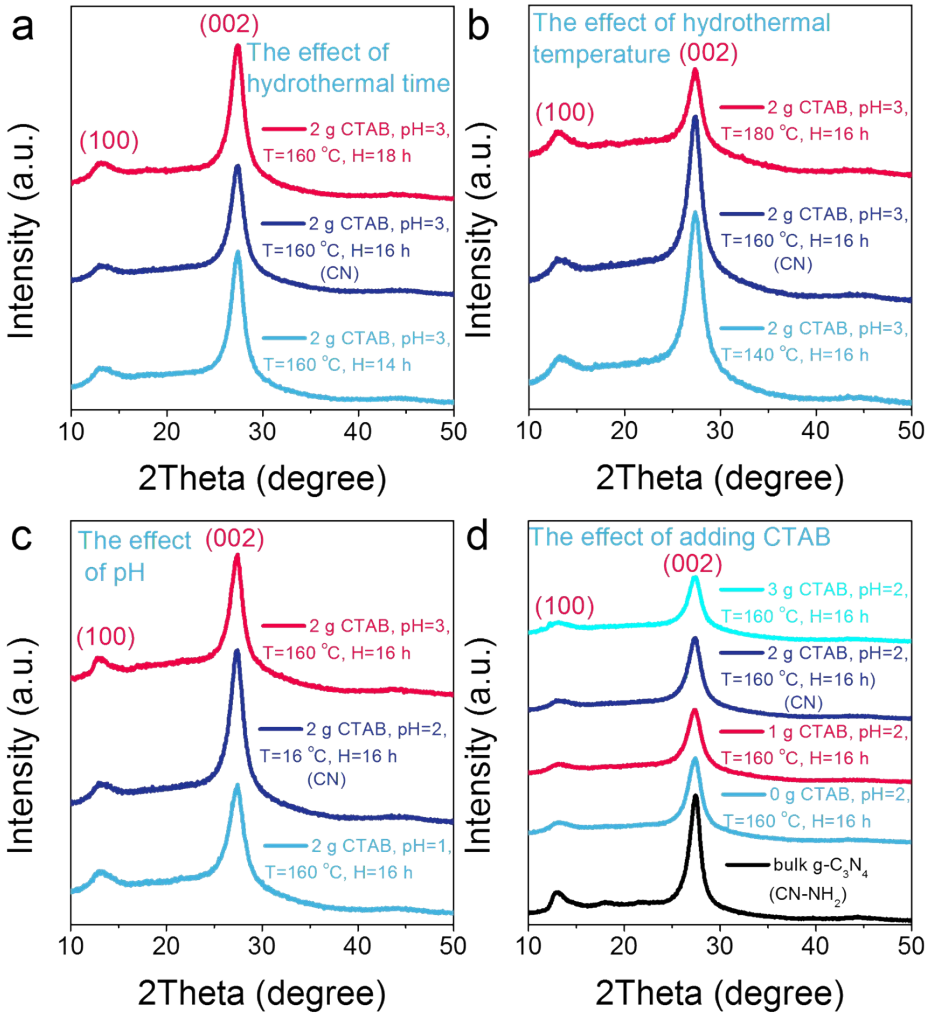

Figure S3. XRD patterns of samples synthesized by different condition. a) Controlling the hydrothermal time. **b)** Controlling the hydrothermal temperature. **c)** Controlling the pH value. **d)** Adding the hexadecyl trimethyl ammonium bromide.

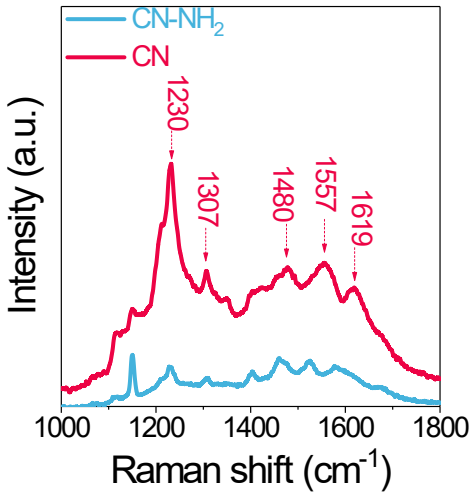

Figure S4. Raman spectra of CN-NH_2 and CN.

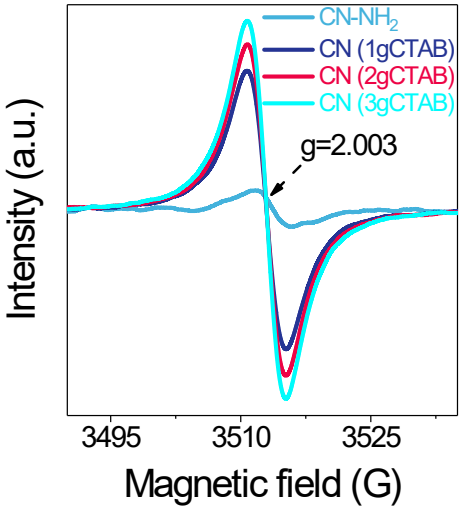

Figure S5. Electron paramagnetic resonance (EPR) spectra affected by adding the CTAB.

Table S1. The peak areas proportions of C-N-H, N-$(C)_3$ and C-N=C based on X-ray photoelectron spectra results.

sample	C-N=C (%)	N-$(C)_3$ (%)	C-N-H (%)	C-N-H/N-$(C)_3$
CN-NH_2	70.31	20.65	9.03	0.44
CN	71.87	20.36	7.77	0.38

Table S2. The peak areas proportions of NH and NH_2 group based on magic angle spinning nuclear magnetic resonance with a H-labelled experiment.

sample	NH_2 (%)	NH (%)
CN-NH_2	59.45	40.54
CN	26.58	73.42

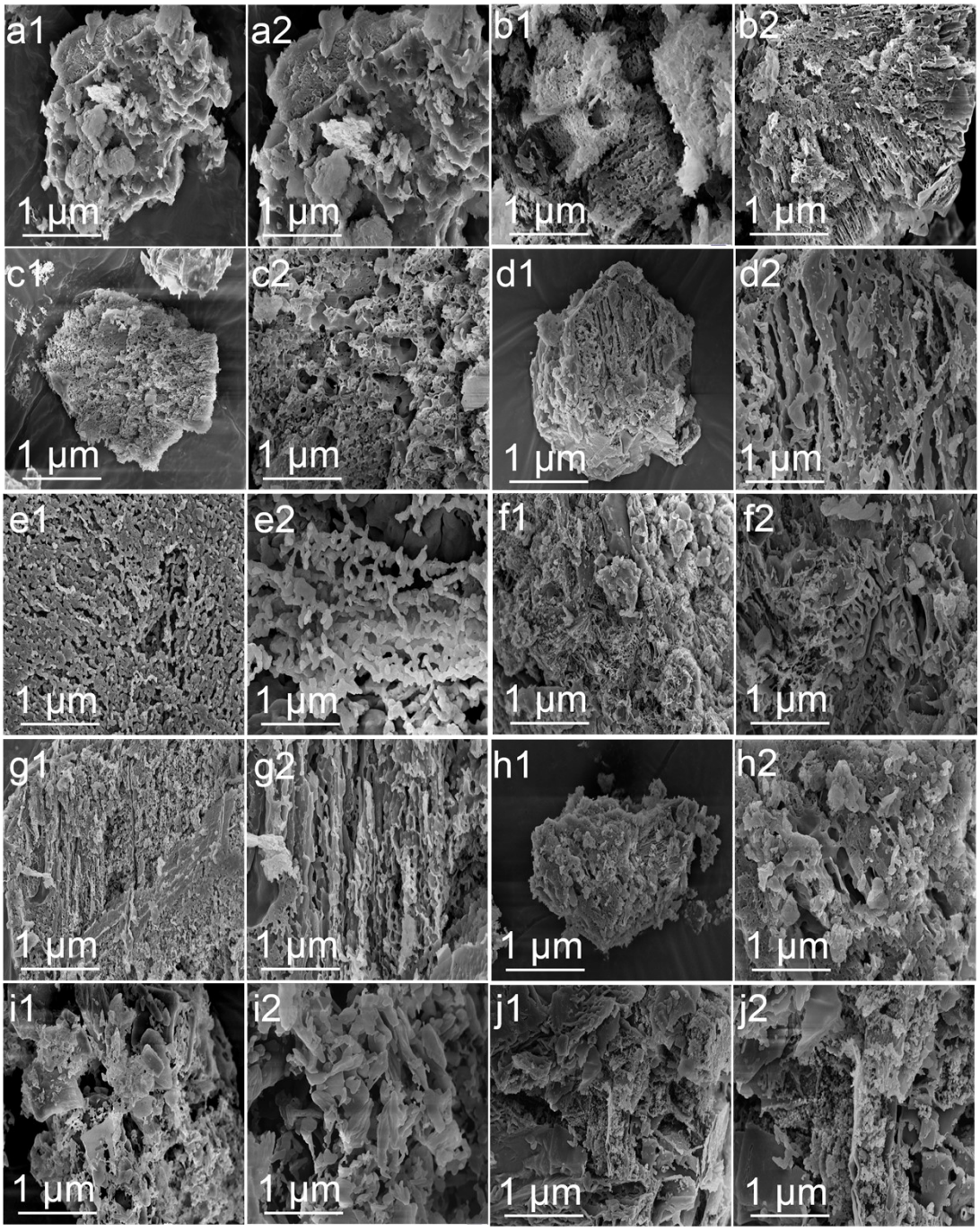

Figure S6. **SEM of porous CN synthesized by different condition, such as the amount of hexadecyl trimethyl ammonium bromide (CTAB), the regulated pH of solution, hydrothermal temperature and time: a1 and a2)** 0 g CTAB, pH=2, T=160 °C and H=16 h. **b1 and b2)** 1 g CTAB, pH=2, T=160 °C and H=16 h. **c1 and c2)** 2 g CTAB, pH=2, T=160 °C and H=16 h. **d1 and d2)** 3 g CTAB, pH=2, T=160 °C and H=16 h. **e1 and e2)** 2 g CTAB, pH=1, T=160 °C and H=16 h. **f1 and f2)** 2 g CTAB, pH=3, T=160 °C and H=16 h. **g1 and g2)** 2 g CTAB, pH=2, T=160 °C and H=14 h. **h1 and h2)** 2 g CTAB, pH=2, T=160 °C and H=18 h. **i1 and i2)** 2 g CTAB, pH=2, T=140 °C and H=16 h. **j1 and j2)** 2 g CTAB, pH=2, T=180 °C and H=16 h.

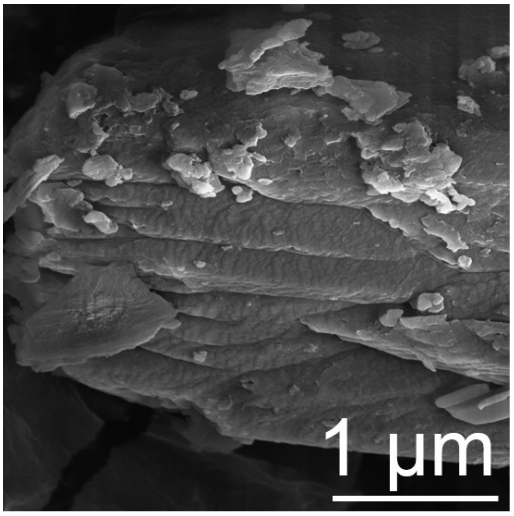

Figure S7. Field-emission scanning electron microscope (FESEM) images of CN-NH_2.

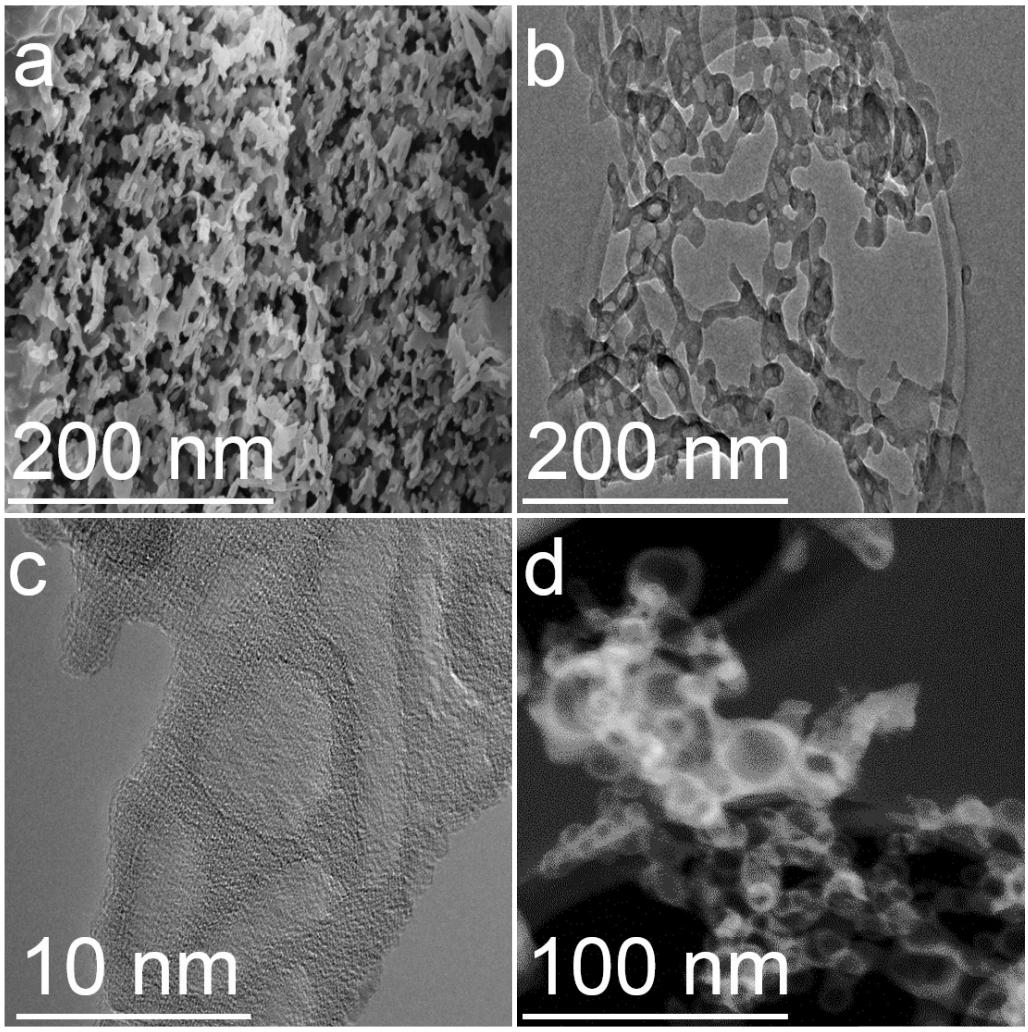

Figure S8. Physical morphology and porous properties of CN. a) Field-emission scanning electron microscope (FESEM) image. **b)** Transmission electron microscope (TEM). **c)** High resolution transmission electron microscope (HRTEM). **d)** Scanning transmission electron microscope (STEM).

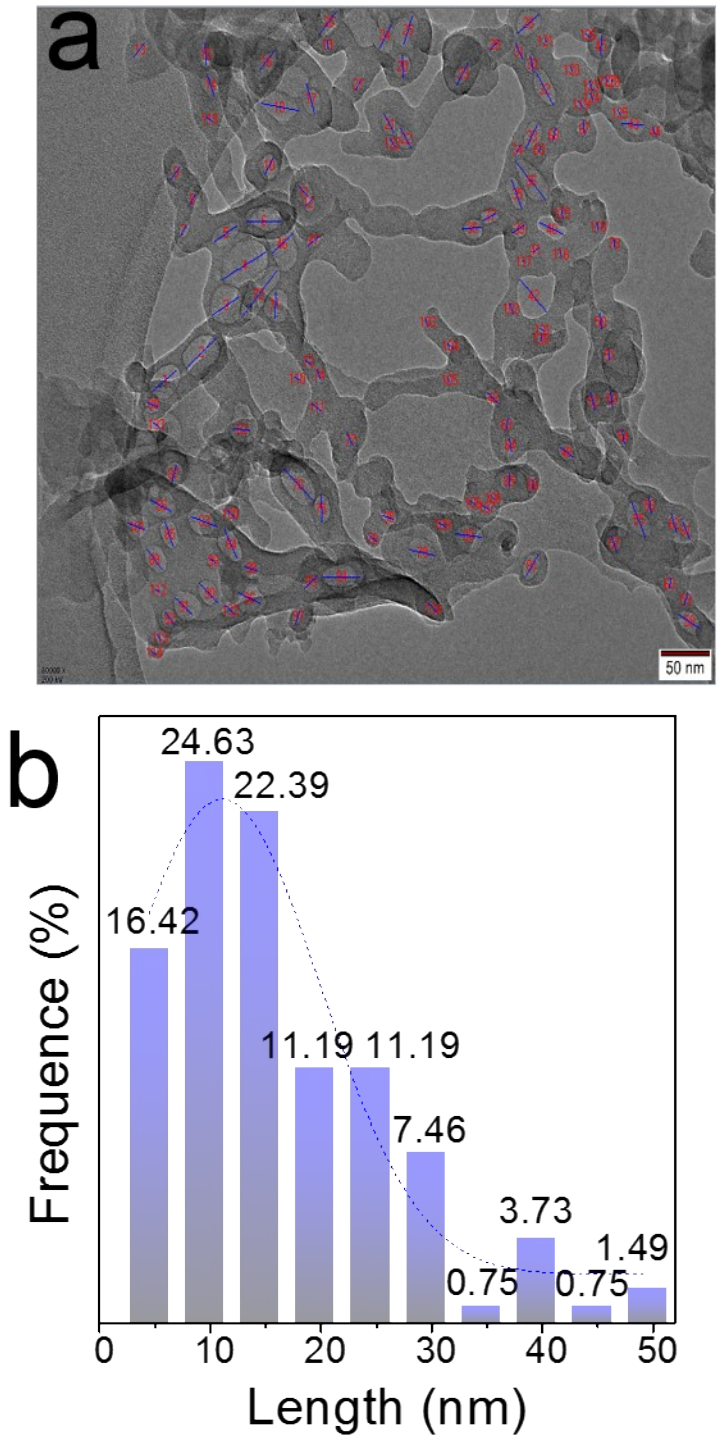

Figure S9. The pore size distribution of porous CN: a) The selected areas for pore size statistics, **b)** the result of measured pore size distribution.

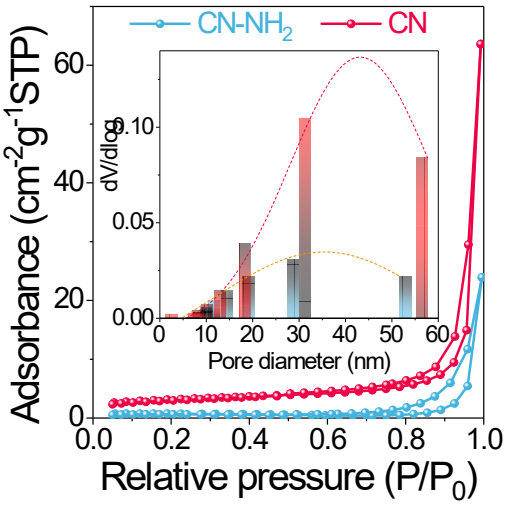

Figure S10. Nitrogen adsorption-desorption isotherm and pore size distribution.

Table S3. Nanoparticle size of CN-NH_2 and CN.

sample	Nanoparticle size (nm)
CN-NH_2	1030 - 4160
CN	160 - 710

Table S4. BET specific surface area and pore size of CN-NH_2 and CN.

sample	BET specific surface area (m^2 g^{-1})	Pore size (nm)
CN-NH_2	2.02	43.69
CN	10.51	45.50

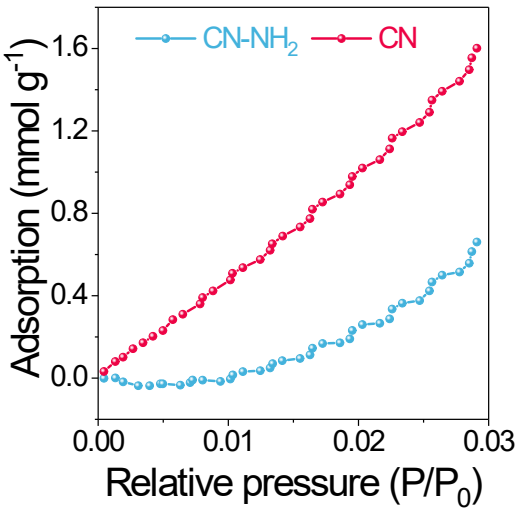

Figure S11. CO_2 adsorption isotherms at 273.15 K.

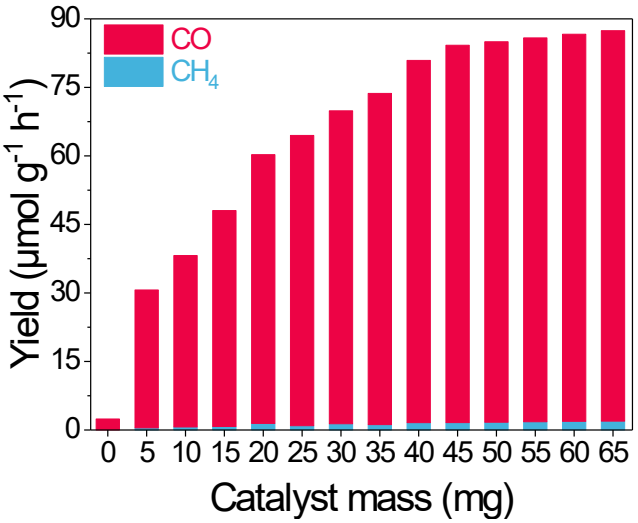

Figure S12. Photocatalytic performance of CN with different catalyst mass.

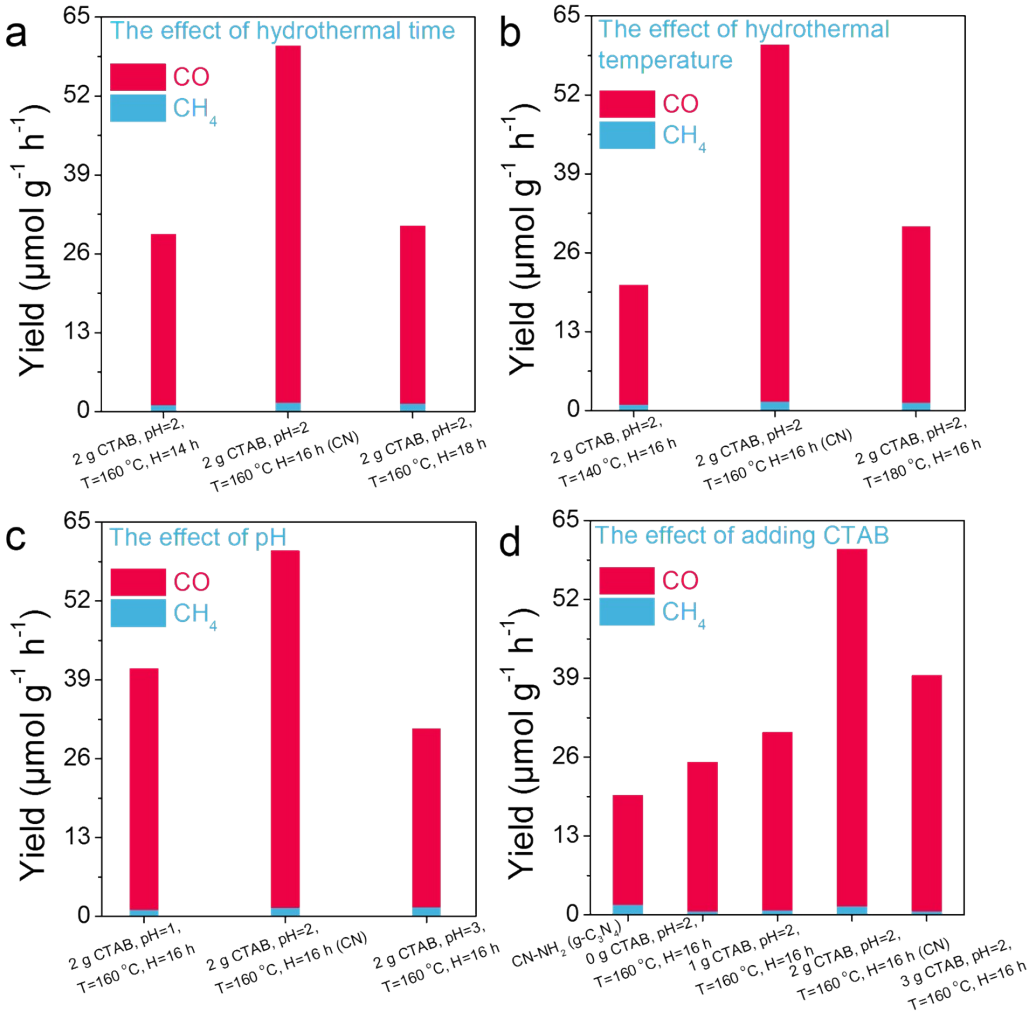

Figure S13. Photocatalytic performance of samples synthesized by different conditions. **a)** The effect of hydrothermal time. **b)** The effect of hydrothermal temperature. **c)** The effect of regulating pH. **d)** The effect of adding CTAB.

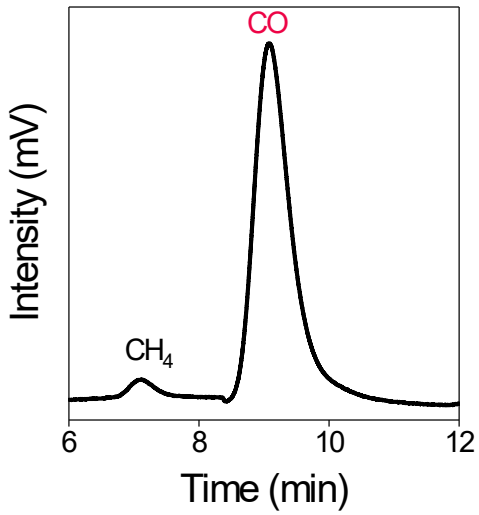

Figure S14. The CH_4 and CO signals collected by gas chromatography for confirming the CH_4 and CO productions.

Table S5. Comparison of CO_2 photoreduction performance with other photocatalysts.

Sample	Light source	Products	Main product rate (CO)	Main product selectivity (CO)	Reference
$CN\text{-}NH_2$	300 W Xe lamp	CH_4, CO	18.07 μmol g^{-1} h^{-1}	91.52%	**This work**
CN	300 W Xe lamp	CH_4, CO	58.83 μmol g^{-1} h^{-1}	97.61%	**This work**
$TiO_2/CsPbBr_3$	300 W Xe lamp	H_2, CO	9.02 μmol g^{-1} h^{-1}	95 %	[1]
$Bi_4Ti_3O_{12}$	300 W Xe lamp	CO	15.1 μmol g^{-1} h^{-1}	/	[2]
$BiOIO_3$ with surface oxygen vacancies	300 W Xe lamp	H_2, CH_4, CO	17.33 μmol g^{-1} h^{-1}	/	[3]
$Br\text{-}Bi_2O_2(OH)(NO_3)$	300 W Xe lamp	CH_4, CO	8.12 μmol g^{-1} h^{-1}	/	[4]
CoRu-HCNp	300 W Xe lamp	CH_4, CO	27.31 μmol g^{-1} h^{-1}	91.8 %	[5]
$Cu/g\text{-}C_3N_4$	300 W Xe lamp	CH_4, CO	3.1 μmol g^{-1} h^{-1}	~100%	[6]
$LaPO_4/g\text{-}C_3N_4$	300 W Xe lamp	CO	14.4 μmol g^{-1} h^{-1}	/	[7]
Ni/Porous few layer $g\text{-}C_3N_4$	300 W Xe lamp	CH_4, CO	8.6 μmol g^{-1} h^{-1}	81.1%	[8]
R-CNS-400	300 W Xe lamp	CO, CH_4, and C_2H_4	55.3 μmol g^{-1} h^{-1}	98.9 %	[9]
CCN	300 W Xe lamp	CO, CH_4, CH_3OH, and CH_3CH_2OH	12.1 μmol g^{-1} h^{-1}	91.5 %	[10]
Cu/CN-0.25	300 W Xe lamp	CO, CH_4, and CH_3OH	11.2 μmol g^{-1} h^{-1}	82.6 %	[11]
Ni/CN-0.5	300 W Xe lamp	CO, CH_4	19.9 μmol g^{-1} h^{-1}	81.22%	[12]
0.7Ni-5OB-CN	300 W Xe lamp	CO, CH_4	22.1 μmol g^{-1} h^{-1}	71.75%	[13]
CoNiSx-CN	300 W Xe lamp	CO, CH_4	11.77 μmol g^{-1} h^{-1}	92.86 %	[14]
$g\text{-}C_3N_4/TiO_2/C$	300 W Xe lamp	CO, CH_4	8.65 μmol g^{-1} h^{-1}	87.52%	[15]
$P\text{-}CeO_2/g\text{-}C_3N_4$	300 W Xe lamp	CO	0.523 μmol g^{-1} h^{-1}	100%	[16]
Ni/S-CN-N	300 W Xe lamp	CO, CH_4	11.72 μmol g^{-1} h^{-1}	75.61%	[17]

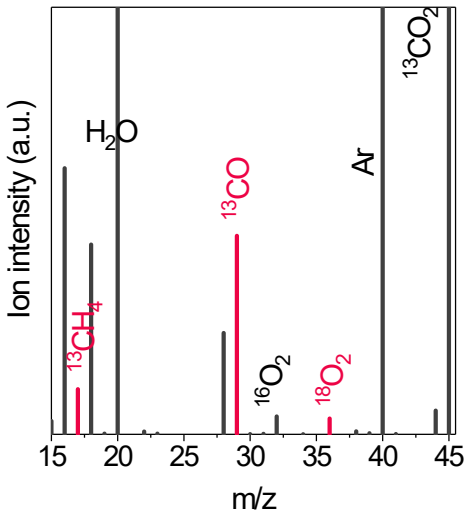

Figure S15. The isotope tracer experiment of H_2O oxidation (The volume ratio between $H_2{}^{16}O$ and $H_2{}^{18}O$ is 1 : 1).

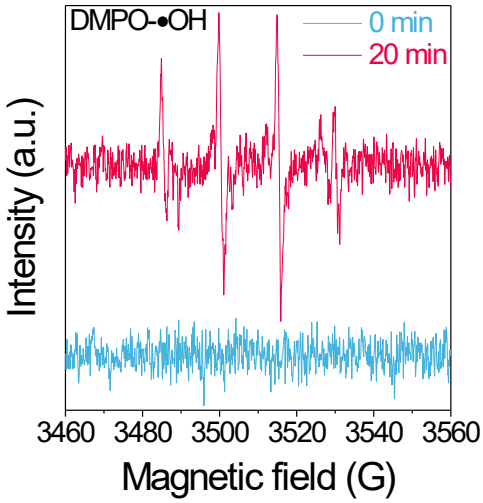

Figure S16. Electron paramagnetic resonance signal of CN. DMPO-•OH signal detected in dark condition and light irradiation for 20 min.

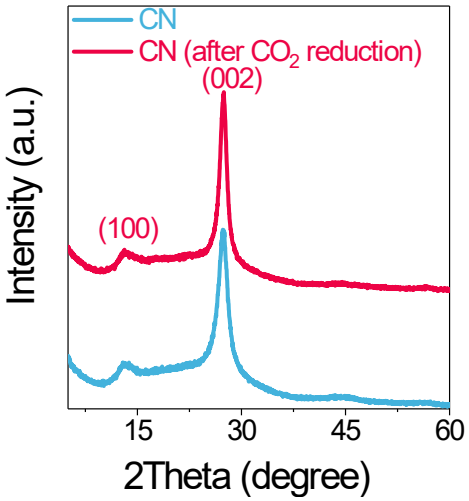

Figure S17. X-ray diffraction (XRD) pattern of CN and CN after CO_2 photoreduction.

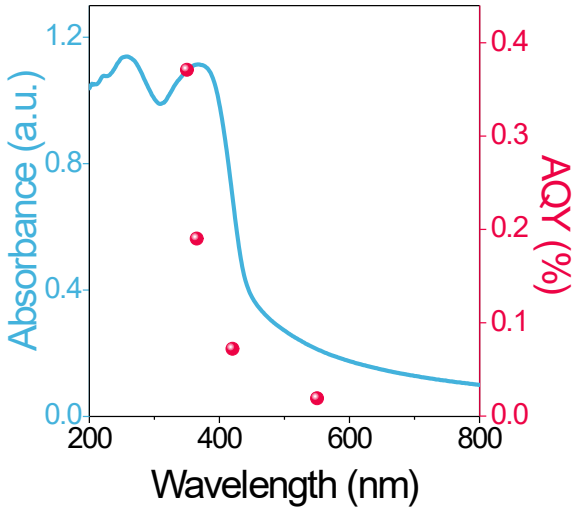

Figure S18. Absorbance and apparent quantum yield (AQY).

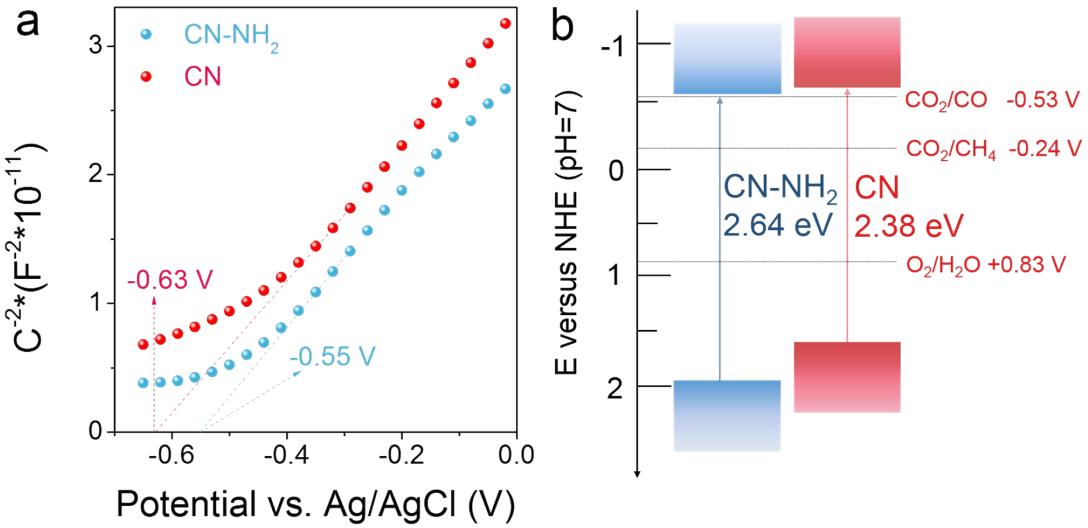

Figure S19. **Redox potential: a)** Reductive potentials obtained from Mott-Schottky plots and **b)** schematics illustrating the electronic band structures and redox potentials.

The band structures are important for CO_2 photoreduction[18]. The Mott-Schottky tests indicated that both CN-NH_2 and CN had positive slopes, suggesting that both CN-NH_2 and CN were typical *n*-type semiconductor (Figure S14a). The flat-band potentials of CN-NH_2 and CN were -0.55 and -0.63 V, respectively. Generally, the conduction band minimum (CBM) of *n*-type semiconductor was closed to its flat-band potential[19,20]. Thus, the CBM of CN-NH_2 and CN were about -0.55 and -0.63 V vs. NHE, which was close to other reports[21-23]. Moreover, based on the $E_{VB} = E_{CB} + E_g$, the valance band minimum (VBM) of CN-NH_2 and CN were 2.09 and 1.75 V vs. NHE. Thus, the band structures and redox potentials of CO_2 reduction suggested that the CN-NH_2 and CN had suitable band structures for realizing CO_2 reduction (Figure S14b).

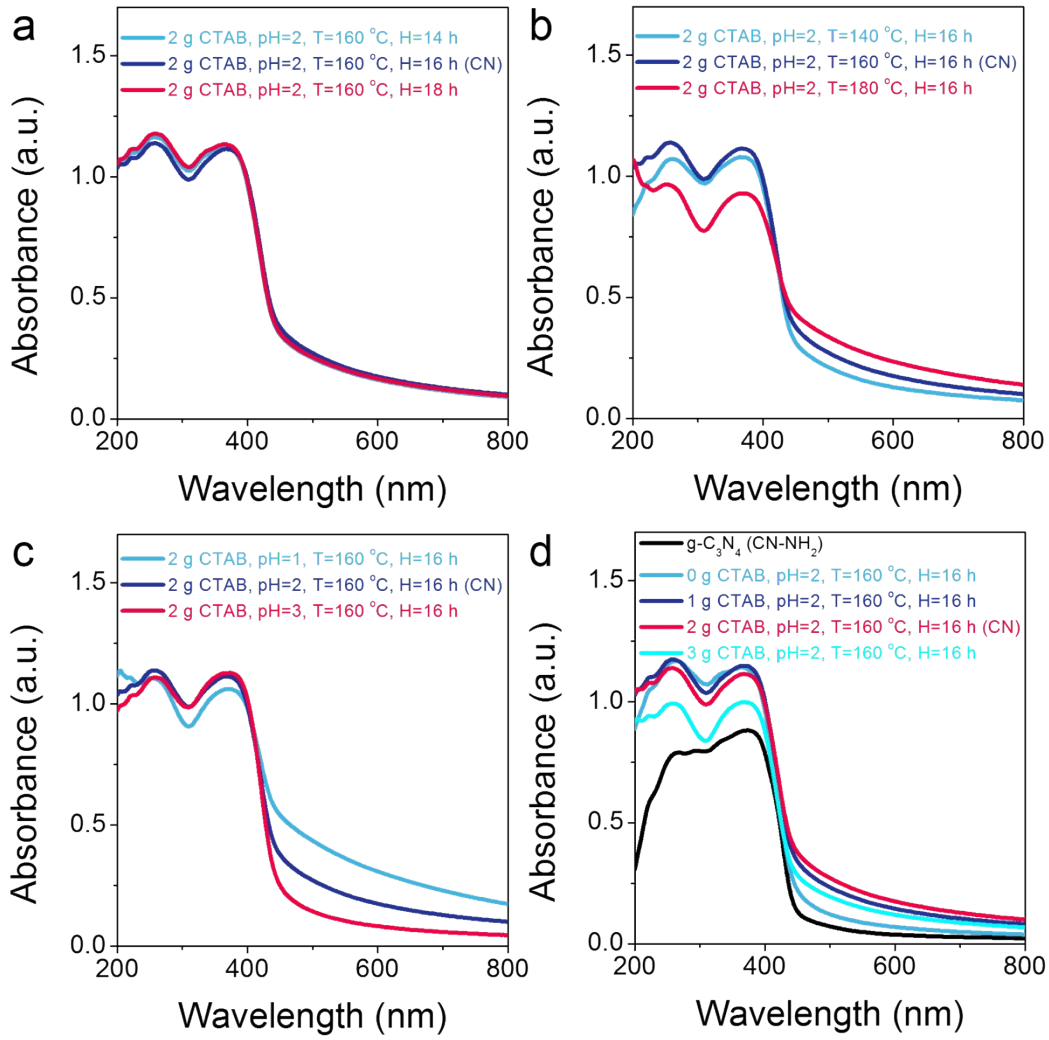

Figure S20. UV-vis diffuse reflectance spectra of samples synthesized by different condition. **a)** Controlling the hydrothermal time. **b)** Controlling the hydrothermal temperature. **c)** Controlling the pH value. **d)** Adding the hexadecyl trimethyl ammonium bromide.

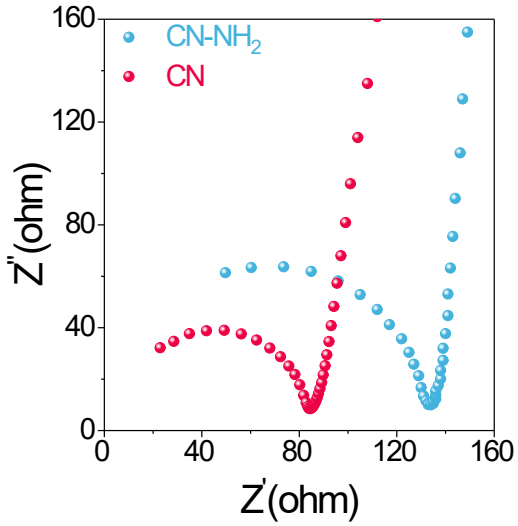

Figure S21. Electrochemical impedance spectroscopy (EIS) of CN and CN-NH_2.

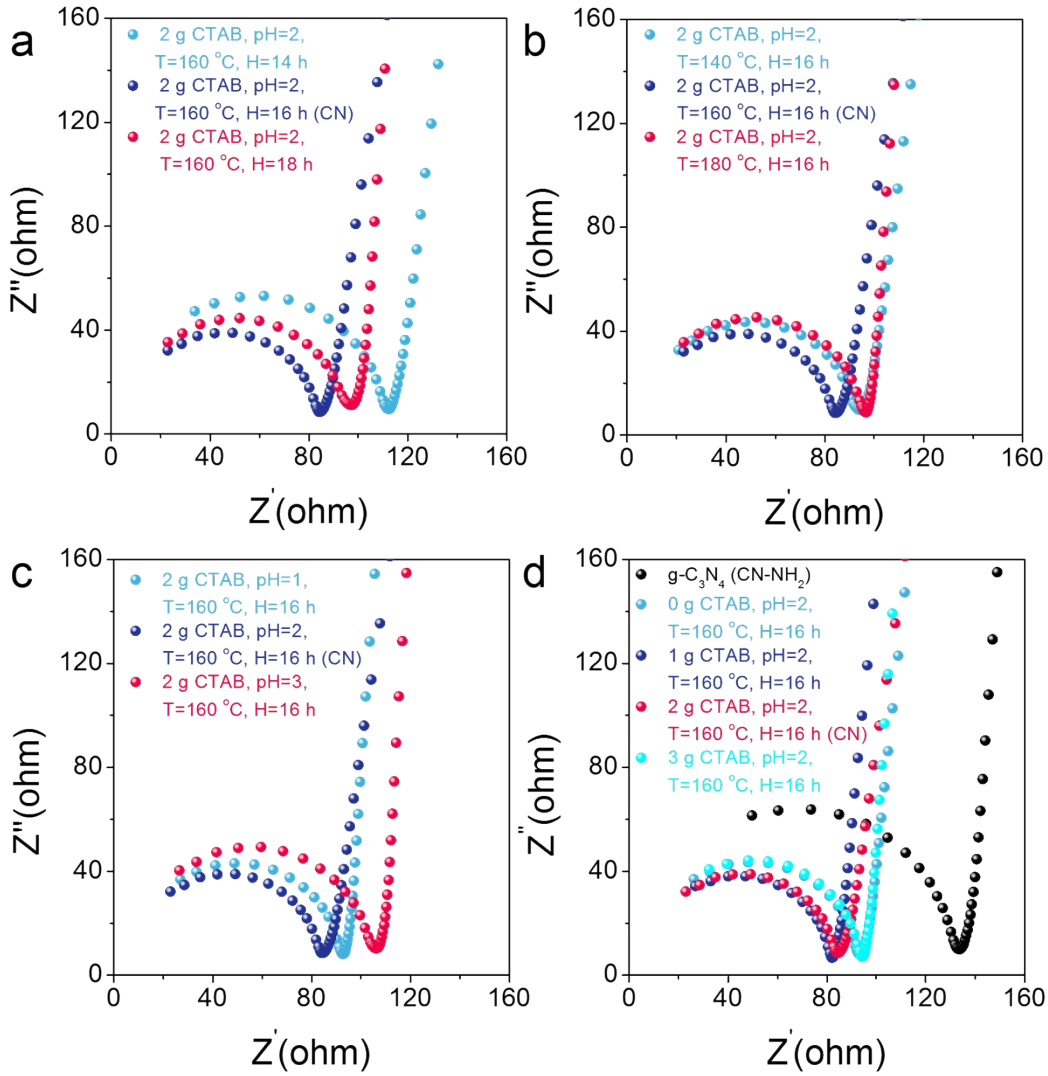

Figure S22. EIS of samples synthesized by different condition. a) Controlling the hydrothermal time. **b)** Controlling the hydrothermal temperature. **c)** Controlling the pH value. **d)** Adding the hexadecyl trimethyl ammonium bromide.

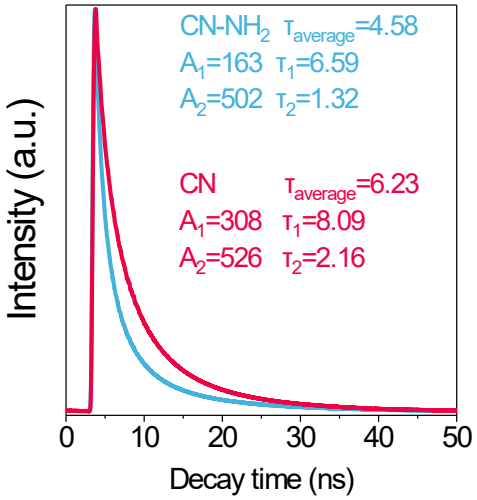

Figure S23. Time-resolved transient fluorescence decay spectra of CN and CN-NH_2.

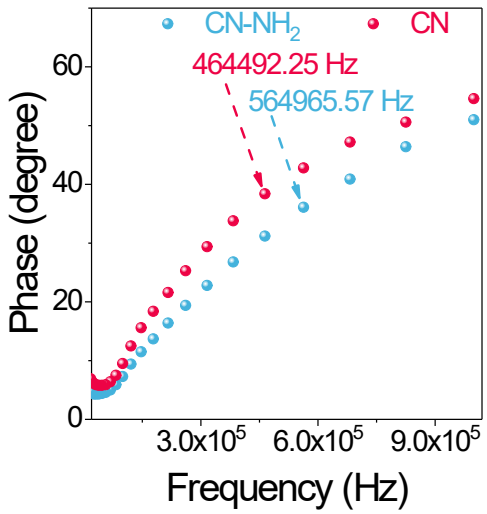

Figure S24. Bode phase spectra of CN and CN-NH_2..

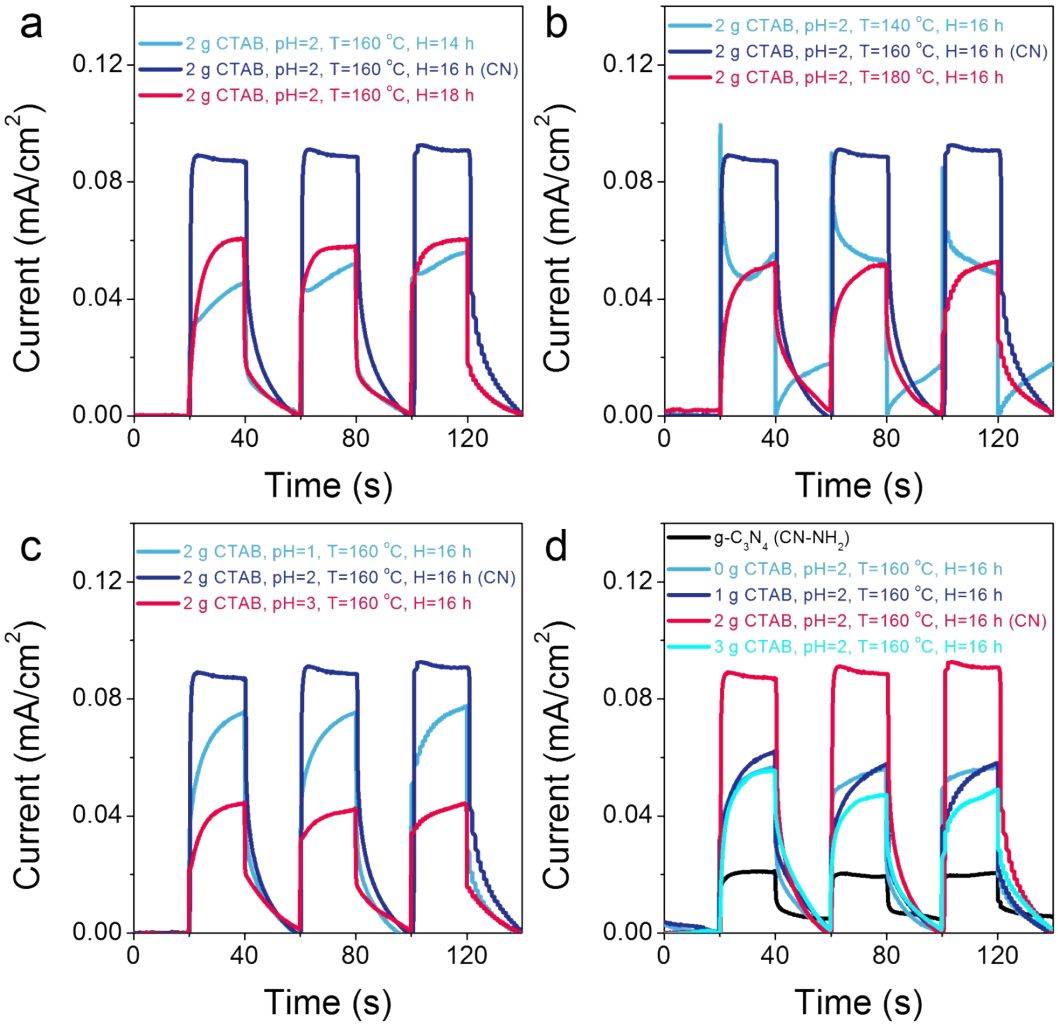

Figure S25. Transient photocurrent response of samples synthesized by different condition. a) Controlling the hydrothermal time. **b)** Controlling the hydrothermal temperature. **c)** Controlling the pH value. **d)** Adding the hexadecyl trimethyl ammonium bromide.

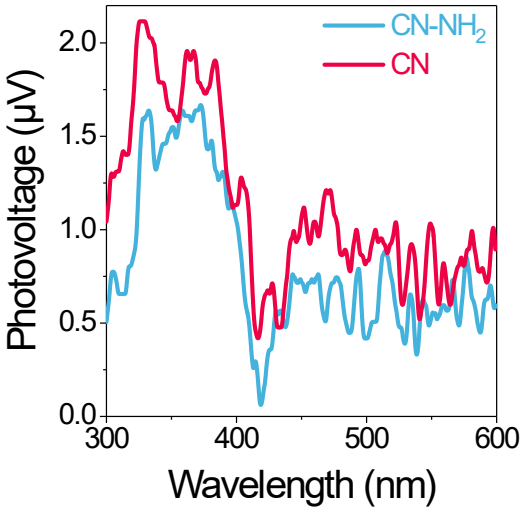

Figure S26. Photovoltage of CN-NH_2 and CN.

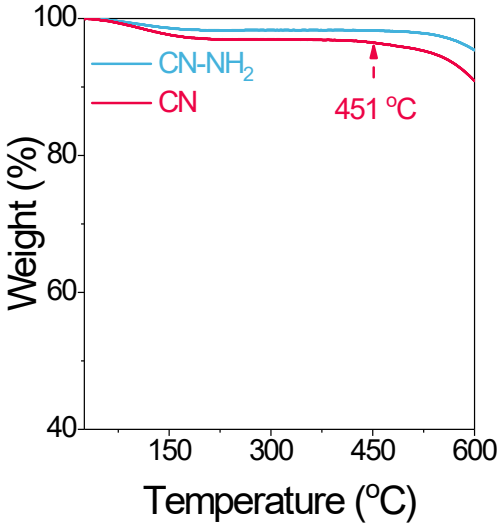

Figure S27. Thermogravimetry analysis.

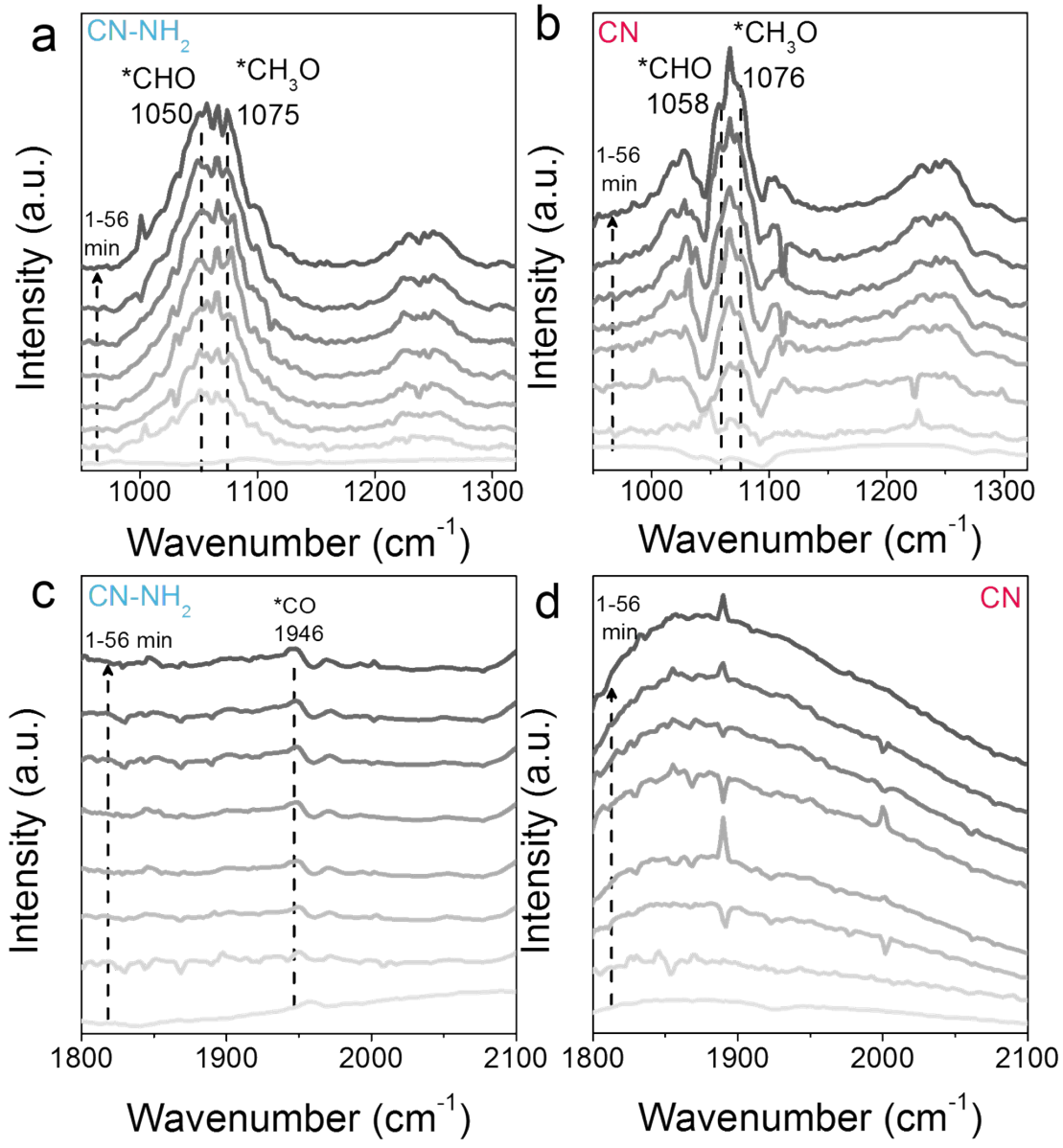

Figure S28. *In-situ* Fourier-transform infrared (*In-situ* FTIR) spectra of CO_2 photoreduction. **a, c)** CN-NH_2**, b, d)** CN

Table S6. The peak areas of adsorbed H_2O, carbonates and adsorbed CO_2 based on XPS results.

sample	Adsorbed H_2O (CPS.eV)	Carbonates (CPS.eV)	Adsorbed CO_2 (CPS.eV)
CN-NH_2	4149.16	6508.57	1502.39
CN	4248.82	7701.19	5373.94

Table S7. BET specific surface area, pore size, and nanoparticle size of CN-NH_2 and CN.

sample	BET specific surface area (m^2 g^{-1})	CO production rate (μmol g^{-1} h^{-1})	CO production rate/BET specific surface area (μmol h^{-1} m^{-2})
CN-NH_2	2.02	18.07	8.94
CN	10.51	58.83	5.59

Table S8. The mass content of nitrogen, carbon and hydrogen.

sample	N (wt %)	C (wt %)	H (wt %)
CN-NH_2	60.96	33.96	2.103
CN	59.04	34.14	1.807

The molar amount of nitrogen in CN-NH_2 = {[mass content of nitrogen (wt %)]×[catalyst mass (g)]} / { nitrogen relative atomic mass (14.007)}= {60.96%×0.02g}/14.007= 8.704×10^{-4} mol.

The molar amount of carbon in CN-NH_2 = {[mass content of carbon (wt %)]×[catalyst mass (g)]} / {carbon relative atomic mass (12.011)}= {33.96%×0.02g}/12.011= 5.654×10^{-4} mol.

The molar amount of hydrogen in CN-NH_2 = {[mass content of hydrogen (wt %)]×[catalyst mass (g)]} / {hydrogen relative atomic mass (1.008)}= {2.103%×0.02g}/1.008= 4.173×10^{-4} mol.

The molar amount of nitrogen in CN = {[mass content of nitrogen (wt %)]×[catalyst mass (g)]} / {nitrogen relative atomic mass (14.007)}= {59.04%×0.02g}/14.007= 8.43×10^{-4} mol.

The molar amount of carbon in CN = {[mass content of carbon (wt %)]×[catalyst mass (g)]} / {carbon relative atomic mass (12.011)}= {34.14%×0.02g}/12.011= 5.685×10^{-4} mol.

The molar amount of hydrogen in CN = {[mass content of hydrogen (wt %)]×[catalyst mass (g)]} / {hydrogen relative atomic mass (1.008)}= {1.807%×0.02g}/1.008= 3.585×10^{-4} mol.

Table S9. The molar amount of nitrogen, carbon and hydrogen in 0.02 g catalyst.

sample	N (mol)	C (mol)	H (mol)	Catalytic sites (mol)
CN-NH_2	8.704×10^{-4}	5.654×10^{-4}	4.173×10^{-4}	4.173×10^{-4}
CN	8.43×10^{-4}	5.685×10^{-4}	3.585×10^{-4}	5.88×10^{-5}
The difference between CN-NH_2 and CN			5.88×10^{-5}	

To reveal the relationship between molar amount of catalytic sites and photocatalytic performance, the elemental analysis was conducted to calculate the molar amount of catalytic sites (Table S8 and Table S9). The molar amount of hydrogen in 0.2 g CN-NH_2 was 4.173×10^{-4} mol, implying that the -NH_2 group was 2.087×10^{-4} mol. There were two catalytic sites (nitrogen atoms) adjacent to the -NH_2 group, implying that the molar amount of catalytic sites in CN-NH_2 was 4.173×10^{-4} mol. The CO production rate of CN-NH_2 was 18.07 μmol g^{-1} h^{-1}, thus, CO production rate of CN-NH_2 was 43302.18 μmol $g_{catalytic\ site}^{-1}$ h^{-1}. Importantly, the molar amount of lost hydrogen in 0.2 g CN was 5.88×10^{-5} mol, implying that the molar amount of lost -NH_2 group was 2.94×10^{-5} mol. There were two catalytic sites (nitrogen atoms) adjacent to the lost -NH_2 group, implying that the molar amount of catalytic sites in CN was 5.88×10^{-5} mol. The CO production rates of CN was 58.83 μmol g^{-1} h^{-1}, thus, CO production rate of CN was 1000510.20 μmol $g_{catalytic\ site}^{-1}$ h^{-1}, respectively.

Table S10. The turnover number (TON) and turnover frequency (TOF) of CO.

sample	Reaction time (h)	Yield of CO (mol)	Catalytic sites (mol)	TON[a]	TOF[b]
CN-NH_2	3	1.08×10^{-6}	4.173×10^{-4}	2.598×10^{-3}	8.659×10^{-4}
CN	3	3.53×10^{-6}	5.88×10^{-5}	6.003×10^{-2}	2.001×10^{-2}

[a]Turnover number (TON) = [mol (product)]/[mol (catalytic sites)].

[b]Turnover frequency (TOF) = [mol (product)]/[mol (catalytic sites)×(reaction time)].

Reference

[1] Xu F, Meng K, Cheng B, et al. Unique S-scheme heterojunctions in self-assembled TiO_2/$CsPbBr_3$ hybrids for CO_2 photoreduction[J]. Nature communications, 2020, 11(1): 1-9.

[2] Liu L, Huang H, Chen Z, et al. Synergistic polarization engineering on bulk and surface for boosting CO_2 photoreduction[J]. Angewandte Chemie International Edition, 2021, 60(33): 18303-18308.

[3] Chen F, Ma Z, Ye L, et al. Macroscopic spontaneous polarization and surface oxygen vacancies collaboratively boosting CO_2 photoreduction on $BiOIO_3$ single crystals[J]. Advanced Materials, 2020, 32(11): 1908350.

[4] Hao L, Kang L, Huang H, et al. Surface‐halogenation‐induced atomic‐site activation and local charge separation for superb CO_2 photoreduction[J]. Advanced Materials, 2019, 31(25): 1900546.

[5] Cheng L, Yue X, Wang L, et al. Dual‐Single‐Atom Tailoring with Bifunctional Integration for High‐Performance CO_2 Photoreduction[J]. Advanced Materials, 2021, 33(49): 2105135.

[6] Li Y, Li B, Zhang D, et al. Crystalline carbon nitride supported copper single atoms for photocatalytic CO_2 reduction with nearly 100% CO selectivity[J]. ACS nano, 2020, 14(8): 10552-10561.

[7] Li M, Zhang L, Fan X, et al. Core-shell $LaPO_4$/g-C_3N_4 nanowires for highly active and selective CO_2 reduction[J]. Applied Catalysis B: Environmental, 2017, 201: 629-635.

[8] Cheng L, Yin H, Cai C, et al. Single Ni atoms anchored on porous few‐layer g‐C_3N_4 for photocatalytic CO_2 reduction: the role of edge confinement[J]. Small, 2020, 16(28): 2002411.

[9] Liu Z, Zhao Z, Jiang W, et al. Structural reconstruction of carbon nitride with tailored electronic structure: A bifunctional photocatalyst for cooperative artificial photosynthesis and selective phenylcarbinol oxidation[J]. Applied Catalysis B: Environmental, 2021, 298: 120517.

[10] Xia P, Antonietti M, Zhu B, et al. Designing defective crystalline carbon nitride to enable selective CO_2 photoreduction in the gas phase[J]. Advanced Functional Materials, 2019, 29(15): 1900093.

[11] Wang J, Heil T, Zhu B, et al. A single Cu-center containing enzyme-mimic enabling full photosynthesis under CO_2 reduction[J]. ACS nano, 2020, 14(7): 8584-8593.

[12] Tang R, Wang H, Zhang S, et al. A ball milling method for highly dispersed Ni atoms on g-C_3N_4 to boost CO_2 photoreduction[J]. Journal of Colloid and Interface Science, 2023, 630: 290-300.

[13] Wang Y, Qu Y, Qu B, et al. Construction of Six-Oxygen-Coordinated Single Ni Sites on g-C_3N_4 with Boron-Oxo Species for Photocatalytic Water-Activation-Induced CO_2 Reduction[J]. Advanced materials, 2021, 33(48): 2105482.

[14] Li F, Huang Y, Gao C, et al. The enhanced photo-catalytic CO_2 reduction performance of g-C_3N_4 with high selectivity by coupling $CoNiS_x$[J]. Materials Research Bulletin, 2021, 144: 111488.

[15] Yang Y, Zhang D, Fan J, et al. Construction of an ultrathin S-scheme heterojunction based on few-layer g-C_3N_4 and monolayer $Ti_3C_2T_x$ MXene for photocatalytic CO_2 reduction[J]. Solar RRL, 2021, 5(2): 2000351.

[16] Li W, Jin L, Gao F, et al. Advantageous roles of phosphate decorated octahedral CeO_2 {111}/g-C_3N_4 in boosting photocatalytic CO_2 reduction: Charge transfer bridge and Lewis basic site[J]. Applied Catalysis B: Environmental, 2021, 294: 120257.

[17] Xu J, Chen Y, Chen M, et al. In situ growth strategy synthesis of single-atom nickel/sulfur co-doped g-C_3N_4 for efficient photocatalytic tetracycline degradation and CO_2 reduction[J]. Chemical Engineering Journal, 2022, 442: 136208.

[18] Matsumoto Y. Energy positions of oxide semiconductors and photocatalysis with iron complex oxides[J]. Journal of Solid State Chemistry, 1996, 126(2): 227-234.

[19] Li P, Li J, Feng X, et al. Metal-organic frameworks with photocatalytic bactericidal activity for integrated air cleaning[J]. Nature communications, 2019, 10(1): 2177.

[20] Wu P, Dai S, Chen G, et al. Interfacial effects in hierarchically porous α-MnO_2/Mn_3O_4 heterostructures promote photocatalytic oxidation activity[J]. Applied Catalysis B: Environmental, 2020, 268: 118418.

[21] Mohamed N A, Safaei J, Ismail A F, et al. Fabrication of exfoliated graphitic carbon nitride,(g-C_3N_4) thin film by methanolic dispersion[J]. Journal of Alloys and Compounds, 2020, 818: 152916.

[22] Wu F, Ma Y, Hu Y H. Near infrared light-driven photoelectrocatalytic water splitting over P-doped g-C_3N_4[J]. ACS Applied Energy Materials, 2020, 3(11): 11223-11230.

[23] Duan S F, Tao C L, Geng Y Y, et al. Phosphorus-doped Isotype g-C_3N_4/g-C_3N_4: An Efficient Charge Transfer System for Photoelectrochemical Water Oxidation[J]. ChemCatChem, 2019, 11(2): 729-736.